

Plasmonic Gold Nanocrystals Coupled with Photonic Crystal Seamlessly on TiO₂ Nanotube Photoelectrodes for Efficient Visible Light Photoelectrochemical Water Splitting

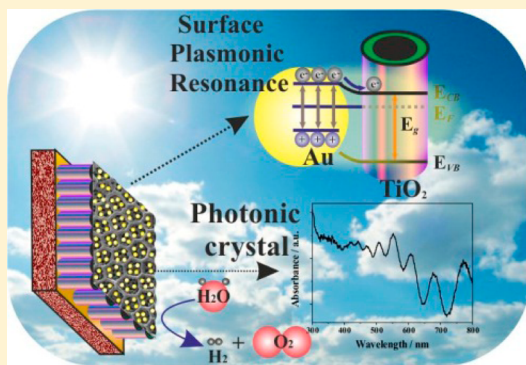
Zhonghai Zhang,[†] Lianbin Zhang,[†] Mohamed Nejib Hedhili,[‡] Hongnan Zhang,[†] and Peng Wang*,[†]

[†]Water Desalination and Reuse Center, Biological and Environmental Science and Engineering Division and [‡]Imaging and Characterization Laboratory, King Abdullah University of Science and Technology, Thuwal 23955-6900, Saudi Arabia

S Supporting Information

ABSTRACT: A visible light responsive plasmonic photocatalytic composite material is designed by rationally selecting Au nanocrystals and assembling them with the TiO₂-based photonic crystal substrate. The selection of the Au nanocrystals is so that their surface plasmonic resonance (SPR) wavelength matches the photonic band gap of the photonic crystal and thus that the SPR of the Au receives remarkable assistance from the photonic crystal substrate. The design of the composite material is expected to significantly increase the Au SPR intensity and consequently boost the hot electron injection from the Au nanocrystals into the conduction band of TiO₂, leading to a considerably enhanced water splitting performance of the material under visible light. A proof-of-concept example is provided by assembling 20 nm Au nanocrystals, with a SPR peak at 556 nm, onto the photonic crystal which is seamlessly connected on TiO₂ nanotube array. Under visible light illumination (>420 nm), the designed material produced a photocurrent density of ~150 $\mu\text{A cm}^{-2}$, which is the highest value ever reported in any plasmonic Au/TiO₂ system under visible light irradiation due to the photonic crystal-assisted SPR. This work contributes to the rational design of the visible light responsive plasmonic photocatalytic composite material based on wide band gap metal oxides for photoelectrochemical applications.

KEYWORDS: Plasmonic, photonic crystal, TiO₂ nanotube, Au nanocrystals, water splitting



Photoelectrochemical (PEC) water splitting is widely regarded as one of the most promising ways for hydrogen generation in the near future, and various semiconductors with controlled nanostructures have been synthesized and investigated as photoelectrodes to alleviate the limitations that generally face all photoelectrocatalysis, i.e., light harvesting, charge separation, carrier mobility, and photostability.^{1–8} Among all the semiconductor materials, TiO₂ remains a favorable choice as photoelectrode material for PEC applications thanks to its remarkable photostability, nontoxicity, and low cost. Recently, one-dimensional nanostructured TiO₂, such as nanorod, nanowire, and nanotube, has received significant attention due to its light confinement, efficient charge separation, and high carrier mobility properties, all of which are beneficial for PEC performance enhancement.^{9–12} Among the one-dimensional TiO₂ nanostructures, TiO₂ nanotube (TiO₂ NT) array fabricated via anodization distinguishes itself owing to its highly ordered, vertically aligned tubular structure, large surface-to-volume ratio, and unidirectional electrical channel.^{13,14}

With the considerable advancement in the morphology control, the limitation coming from the large band gap of TiO₂ (i.e., 3.2 eV for anatase and 3.0 eV for rutile) becomes severe, which limits its optical absorption only within UV light region.

As the UV accounts for only ~4% of the entire solar spectrum, various approaches have been explored to expand TiO₂ optical absorption spectrum into the visible and infrared region. Dye sensitization and nonmetal doping are among the most investigated approaches in this regard,^{15–19} but their effectiveness is limited by either photobleaching of the dye or much reduced electron–hole separation in the presence of nonmetal species in TiO₂ materials. Recently, nanocrystals (NCs) of some noble metals, especially gold (Au), have been attracting much attention because they can strongly interact with light in the visible and infrared region due to their extraordinary localized surface plasmon resonance (SPR) properties and also because of their remarkable photostability.^{20,21} Plasmon resonances arise from the collective oscillations of the electrons close to the surface of the NCs, and the plasmon-excited hot electrons in the noble metal NCs can be transferred to the conduction band of adjacent semiconductor.^{22,23} This desirable plasmonic property of the noble metals has been promoting the concept of assembling plasmonic NCs together with wide band

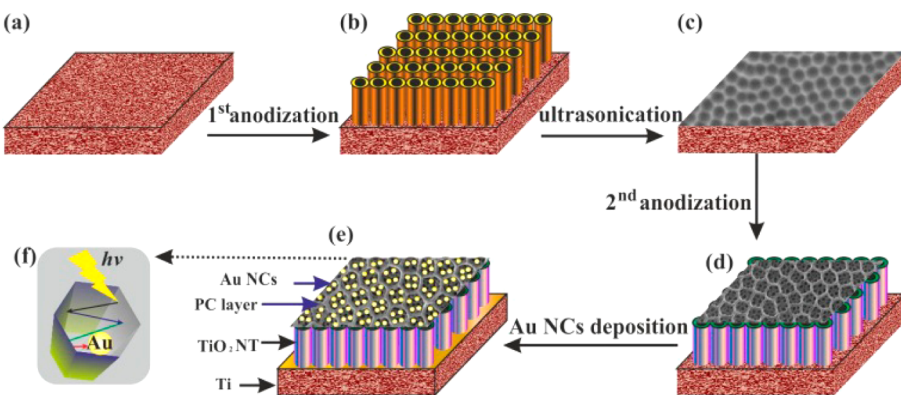
Received: August 6, 2012

Revised: November 5, 2012

Published: December 3, 2012



Scheme 1. Schematic Diagram of the Au/TiO₂ NTPC Fabrication Procedure: (a) Ti Foil; (b) First Anodized TiO₂ NTs; (c) Nanoimprints Left on the Ti Foil after Ultrasonication; (d) Second Anodized TiO₂ NTPC; (e) Au NC Deposition on the TiO₂ NTPC via a Photocatalytic Reduction; (f) Top PC Layer for Light Trapping and Enhancing SPR of the Au NCs



gap metal oxides, especially TiO₂, to produce visible light responsive composite PEC materials. However, so far, the SPR intensity of the plasmonic NCs is still unsatisfactory in the classic plasmonic NCs–TiO₂ composite materials as the light absorption of the composite materials solely relies on the noble metal, and it receives no assistance from the TiO₂ because TiO₂ has little light harvesting capability beyond the UV region.

On the other hand, photonic crystal (PC) is a periodically structured electromagnetic medium, possessing photonic band gaps: ranges of wavelengths usually within visible light range, in which light cannot propagate through the structure and thus is localized and trapped.²⁴ With an aim at enhancing visible light harvesting of semiconductors, the combination of PC layer with certain semiconductor base materials has been investigated.²⁵ However, most of the previous studies in this regard relied on stepwise coating of a PC layer on top of semiconductor materials,^{26–29} which undesirably resulted in poor physical contact and thus high electrical resistance of the thus-produced materials, counterproductive to the designed purpose.

Our group, among others, has recently reported a facile anodization procedure for fabrication of hierarchical TiO₂ NT array,^{30–33} which consists of a periodically well-ordered porous nanostructure on top of a uniform TiO₂ NT array. Naturally, the highly periodically porous top structure motivates us to explore its potential of serving as PC for effective visible light trapping, and the seamless connection between the top porous layer and the bottom tubular array inspires the exploration of this unique structure (denoted as TiO₂ nanotube photonic crystal (TiO₂ NTPC)) as a desirable platform for fabricating visible light responsive TiO₂-based photoelectrode featuring both Au-based plasmonic responses and photonic crystals. Moreover, as the plasmonic wavelengths of Au NCs can be easily tuned, it is thus hypothesized that the SPR intensity of the Au would be remarkably enhanced if the Au plasmonic wavelength can be rationally selected to match the photonic band gap of the TiO₂ NTPC.

This concept, if proven right, would promise a significantly enhanced visible light PEC performance of the thus-prepared TiO₂ composite as with such composite material, the PC layer localizes, traps, and provides multiple paths for the plasmonic wavelength of the Au NCs, which literally magnifies light intensity at this wavelength and thus enhances the SPR of the Au NCs, ultimately leading to enhanced visible light water splitting performance from the TiO₂. The PC-assisted SPR of

the plasmonic NCs would be one of unique advantages of such materials.

The current study is designed to provide a proof for this concept by rationally selecting and assembling the plasmonic Au NCs whose plasmonic wavelength matches the photonic band gap of the TiO₂ NTPC. The thus-prepared materials (Au/TiO₂ NTPC) showed significantly increased visible light PEC water-splitting performance relative to the one without the PC feature. This work thus contributes to the rational design of the visible light responsive plasmonic photocatalytic composite material based on wide band gap metal oxides for photoelectrochemical applications.

Scheme 1 presents the design and fabrication strategy of plasmonic–Au/TiO₂ NTPC photoelectrodes. The detailed synthesis and experimental procedures can be found in the Supporting Information. Briefly, a pristine Ti foil (Scheme 1a) was first anodized and the as-grown TiO₂ NTs (Scheme 1b) were removed by ultrasonication, leaving behind on the surface of the Ti foil well-ordered round concavity imprint pattern (Scheme 1c). The Ti foil with the imprints was then subject to the second anodization to yield uniform TiO₂ NTs with unique hierarchical nanostructure, which consisted of a periodically well-ordered porous top nanostructure sitting on top of a uniform TiO₂ NT array (Scheme 1d). It should be noted that the fabrication procedure of the hierarchical TiO₂ nanostructure in the current study was modified relative to the one reported in our previous publication,³⁰ which did not produce the hierarchical nanostructures with PC light adsorption characteristics. Specifically, the voltages employed in the second anodization were changed from being constant to stepwise increase to compensate for the loss of electric field intensity, which we believe improves periodicity and uniformity of the porous top layer of thus-fabricated hierarchical TiO₂ nanostructure and which are critical factors for forming the top PC layer. The Au NCs were subsequently deposited onto the TiO₂ NTPC by a facile photocatalytic reduction method (Scheme 1e),²² which was judiciously chosen as the plasmonic wavelength of the in situ synthesized Au NCs matched the photonic band gap of the TiO₂ NTPC. As a result, the Au/TiO₂ NTPC are rationally designed so that light with energy matching the photonic band gap of the PC is trapped and localized in the PC layer which reflects and scatters the photon flux that is not directly absorbed by the Au NCs on its first pass. Therefore, the design of the Au/TiO₂ NTPC permits multiple passes for the plasmonically active photons of the Au NCs and

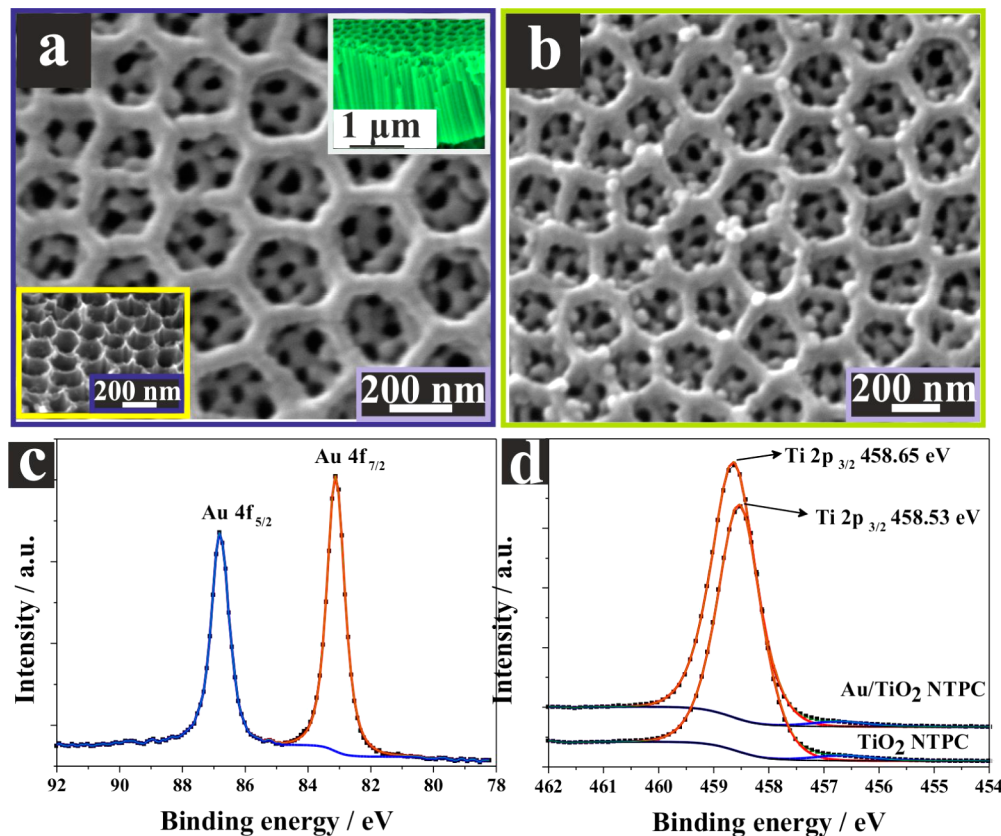


Figure 1. SEM images of (a) TiO_2 NTPC, top right inset shows a cross-section view image and bottom left inset shows high magnification of tilt 15° cross-sectional view of top PC layer; (b) Au/TiO_2 NTPC; high resolution XPS of (c) Au 4f of Au/TiO_2 NTPC and (d) Ti 2p of TiO_2 NTPC and Au/TiO_2 NTPC.

thus increases the average photon path length, which would result in an enhanced SPR intensity of the Au NCs as schematically described in Scheme 1f.

Figure 1a presents a top view scanning electron microscope (SEM) image of the as-prepared TiO_2 NTPC. A top layer with a periodically porous structure is clearly observed, with an average diameter of the pores at ~ 200 nm and a wall thickness of ~ 25 nm. The thickness of the bottom TiO_2 NT layer is about $2 \mu\text{m}$ (top right inset in Figure 1a). It should be noted that the length of the TiO_2 NT in this study was rationally chosen as it has been reported that $2 \mu\text{m}$ is the maximum penetration depth of the incident light in TiO_2 , and any further increase in the tube length would increase its electronic resistance while without the benefit of enhanced light capture.^{10,19,34,35} A tilt 15° cross-sectional SEM view of the TiO_2 NTPC (bottom left inset of Figure 1a) shows a uniformly nonflat, concave-like top layer, which is seamlessly connected with the bottom TiO_2 NT array. The concaves in the PC layer are expected to work as nanomirrors for light reflection and scattering (Scheme 1f). The XRD patterns of the TiO_2 NTPC show vastly dominant anatase phase with preferential orientation of (101) (Figure S1). The top-view SEM image of the Au/TiO_2 NTPC is shown in Figure 1b, which clearly exhibits the well-dispersed Au NCs with average size of around 20 nm. The energy dispersive X-ray spectroscopy (EDS) spectrum of the Au/TiO_2 NTPC presents another evidence of the successful Au deposition (Figure S2). The dominant Au peak in the XRD pattern of the Au/TiO_2 NTPC (Figure S1) could be indexed to the (111) plane. Furthermore, the X-ray photoelectron spectroscopy (XPS) technique was employed to

analyze the specific surface composition of the TiO_2 NTPC and Au/TiO_2 NTPC to acquire in-depth fundamental information on the interaction of Au with TiO_2 . The survey spectra of the TiO_2 NTPC and Au/TiO_2 NTPC can be found in Figure S3, and high-resolution spectra of Au 4f from the Au/TiO_2 NTPC and Ti 2p from the TiO_2 NTPC and Au/TiO_2 NTPC are presented in Figures 1c and 1d, respectively. The Au 4f_{7/2} core level from the Au/TiO_2 NTPC can be fitted with a single peak at a binding energy of 83.1 eV, which is attributed to metallic gold Au^0 . A significant negative shift (ca. 0.9 eV) of the binding energy for Au 4f_{7/2} relative to 84.0 eV of the bulk Au is identified,³⁶ which is due to the electron transfer from oxygen vacancies of the TiO_2 to Au, leading to a lower Au 4f_{7/2} core level binding energy in the Au/TiO_2 NTPC.³⁷ Moreover, a small positive shift of the Ti 2p_{3/2} after Au loading also reveals feasibility of the electron transfer between the Au and TiO_2 NTPC.

Diffuse reflectance UV-vis absorption spectra of the TiO_2 NTPC in air and in ethanol were measured and are presented in Figure 2a. Multiabsorption peaks around 468, 504, 552, 605, 674, and 744 nm can be clearly observed in visible light region in air due to the featured PC structure, which is similar to computer-simulated absorption spectrum (Figure S4a) using the finite-difference time-domain (FDTD) method (the details of the FDTD simulation can be found in the Supporting Information). There is a slight peak shift between the measured and simulated absorption spectra, which supposedly is ascribed to the nanostructure imperfections of the synthesized TiO_2 NTPC. As known, the optical absorption property of PC is strongly affected by the refractive index of a medium.²⁴

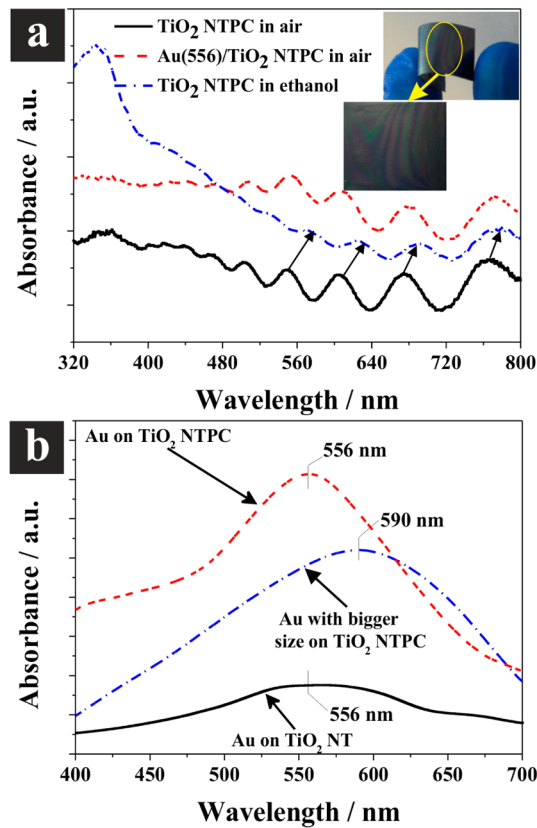


Figure 2. (a) Diffuse reflectance UV-vis absorption spectra of the TiO₂ NTPC in air and in ethanol and Au/TiO₂ NTPC in air. Top right inset is a digital photo of the TiO₂ NTPC to show its flexibility; the middle right inset shows macroscopically visual pattern of the same TiO₂ NTPC; (b) SPR absorption spectra of the Au NCs on the TiO₂ NTPC and TiO₂ NT, with the spectrum of TiO₂ being subtracted.

Compared with air being the medium, an obvious red shift of the absorption peaks was observed with the relative pattern of the absorption peaks remaining when the TiO₂ NTPC was put in ethanol for the same measurement (Figure 2a, blue dashed line). It is worth mentioning that we previously reported that by varying voltages in the two-step anodization the morphology of the hierarchical TiO₂ NT arrays could be finely tuned among nanoring/nanotube, nanopore/nanotube, and nanohole–nanocave/nanotube³⁰ and that the same morphology transition was also identified for the revised synthesis method used in this study. However, among these nanostructures, only the nanoring/nanotube structure showed typical PC light absorption spectra while the nanopore/nanotube and nanohole–nanocave/nanotube failed to produce the same. It is for this reason that the TiO₂ NTPC and Au/TiO₂ NTPC in this study were only limited to the nanoring/nanotube TiO₂ nanostructures. Given the fact that under FDTD simulation all three nanostructures generate typical PC absorption spectra (Figure S4), the reason what causes the discrepancy is unclear and under further investigation.

The top-right inset in Figure 2a shows an actual photo of a TiO₂ NTPC. As the photoelectrodes in this study were fabricated on thin Ti foils (0.125 mm in thickness), they all have a good flexibility. The digital photo in the middle-right inset in Figure 2a shows a visual color pattern on the TiO₂ NTPC photoelectrode, which provides a macroscopic evidence of the formation of a PC layer. The diffuse reflectance UV-vis absorption spectra of the Au/TiO₂ NTPC shows similar multiplexes PC characteristics (Figure 2a, red dashed line), with a significant visible absorption enhancement around 556 nm due to the SPR absorption of the Au NCs at this wavelength (Figure 2b, red dashed line), which was well agreed with the measured SPR wavelength of 558 nm of the same-sized Au NCs dispersed in solution (Figure S5). Among the multi-

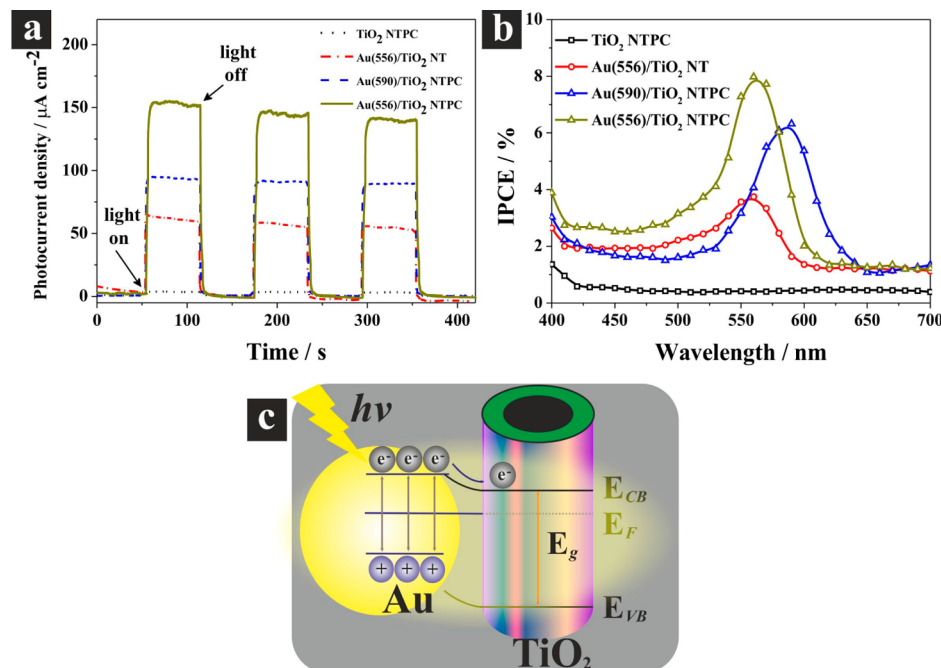


Figure 3. Photoelectrochemical properties of the TiO₂ NTPC and Au/TiO₂ NTPC and schematic diagram of SPR charge carrier transfer mechanisms. (a) Amperometric $I-t$ curves at an applied potential of 1.23 V vs RHE under illumination of visible light with wavelength ≥ 420 nm with 60 s light on/off cycles. (b) IPCE plots in the range of 400–700 nm at 1.23 V vs RHE. (c) SPR charge carrier transfer under a visible light irradiation at Au/TiO₂ interface.

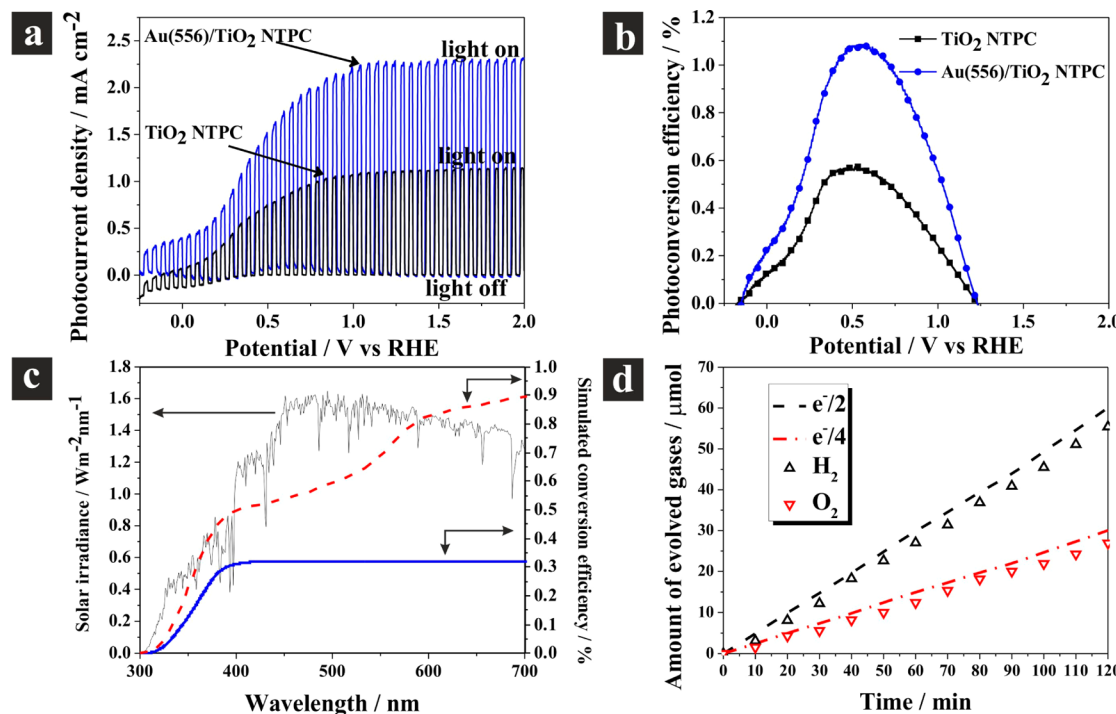


Figure 4. Photoelectrochemical performance of the TiO₂ NTPC and Au(556)/TiO₂ NTPC under entire solar light irradiation (AM 1.5G): (a) linear-sweep voltammograms under chopped illumination, collected with a scan rate of 5 mV s⁻¹; (b) photoconversion efficiency as a function of applied potential; (c) photoconversion efficiency for the Au(556)/TiO₂ NTPC and TiO₂ NTPC as a function of wavelength by integrating their IPCE spectra collected at 0.5 V vs RHE with a standard AM 1.5G solar spectrum (ASTM G-173-03); (d) time courses of gas evolution for the Au(556)/TiO₂ NTPC electrode at 0.5 V vs RHE under illumination of simulated solar light. Note: the e⁻/2 and e⁻/4 represent the theoretical gas volumes calculated from the measured photocurrent density, with e⁻/2 and e⁻/4 being a half and quarter of the electrons passing through the outer circuit, respectively.

absorption peaks of the TiO₂ NTPC, the one around 552 nm is very interesting because it is very close to the maximum resonant wavelength of 556 nm of the Au NCs in the Au/TiO₂ NTPC. The wavelength matching of SPR absorption and PC light trapping would be expected to increase the SPR intensity because the strong localization and trapping of the light by the PC layer would result in a significant enhancement of the light intensity around this region, which can then be specifically garnered by the SPR of the Au NCs. In comparison, the same Au NCs (~20 nm) on the TiO₂ NT without the designed PC layer (SEM images in Figure S6 and DRS spectra in Figure S7) exhibited a much lower SPR intensity (Figure 2b, black solid line). On the other hand, the Au NCs with a bigger size (~40 nm, SEM image in Figure S8) on the same TiO₂ NTPC depicted a red shift of SPR peak at 590 nm (Figure 2b, blue dash-dotted line). In this paper, the samples of the Au/TiO₂ systems with plasmonic wavelength peaks at 556 and 590 nm are denoted with the Au(556)/TiO₂ NT, Au(556)/TiO₂ NTPC, and Au(590)/TiO₂ NTPC. The amounts of the Au NCs present on the Au(556)/TiO₂ NT and Au(556)/TiO₂ NTPC were measured to be comparable, with 0.242 mg cm⁻² on the Au(556)/TiO₂ NT and 0.236 mg cm⁻² on the Au(556)/TiO₂ NTPC, while that on the Au(590)/TiO₂ NTPC was 0.463 mg cm⁻². The fact that the highest SPR intensity among all sample occurred on the Au(556)/TiO₂ NTPC helps prove the design of the material that the SPR intensity of the Au NCs would be enhanced by matching their SPR wavelength with the photonic band gap of the PC. Compared with the Au(556)/TiO₂ NTPC, the poorer SPR intensity on the Au(590)/TiO₂ NTPC, even though it had the

highest amount of the Au NCs among all samples, is ascribed to the mismatch of the plasmonic wavelength and photonic band gap.

To evaluate the enhanced PEC performance under visible light irradiation on the designed plasmonic–photonic crystal system (i.e., Au(556)/TiO₂ NTPC), a set of PEC measurements were carried out. First, chronoamperometric $I-t$ curves were measured and recorded in Figure 3a under illumination of visible light (wavelength ≥ 420 nm) at a constant potential of 1.23 V vs RHE (reversible hydrogen electrode), which is the potential often chosen as a metric to evaluate the performance of photoanodes as it corresponds to the water oxidation potential. Clearly, the TiO₂ NTPC produced little photocurrent density, $< 3 \mu\text{A cm}^{-2}$, which was just above the background dark current. As expected, a significant photocurrent density enhancement was observed on the Au(556)/TiO₂ NTPC, with a photocurrent density of $\sim 150 \mu\text{A cm}^{-2}$ under otherwise the same conditions, which was 50 times the one on the TiO₂ NTPC and was much higher than the photocurrent density of $\sim 60 \mu\text{A cm}^{-2}$ on the Au/TiO₂ NT without a PC layer and $\sim 90 \mu\text{A cm}^{-2}$ on the Au(590)/TiO₂ NTPC. As a matter of fact, the value of $150 \mu\text{A cm}^{-2}$ is the highest ever reported in any plasmonic Au/TiO₂ system under similar irradiation conditions.^{38–41} The much improved photocurrent density on the Au(556)/TiO₂ NTPC relative to the Au(590)/TiO₂ NTPC and Au(556)/TiO₂ NT without a PC layer is ascribed to its enhanced SPR intensity due to the matching of the photonic band gap of the PC layer with the SPR wavelength of the Au NCs, which boosts the PEC performance under visible light irradiation.

To estimate the correlation between SPR light absorption and photocurrent density on the Au/TiO₂ NTPC, incident-photon-to-current-conversion efficiency (IPCE) measurements were performed under a constant potential of 1.23 V vs RHE. IPCE values were calculated using the following equation and are presented in Figure 3b as a function of the incident visible light wavelength:

$$\text{IPCE} (\%) = 1240I/\lambda J_{\text{light}} \times 100\% \quad (1)$$

where I is the photocurrent density (mA cm^{-2}), J_{light} is the incident light irradiance (mW cm^{-2}), and λ is the incident light wavelength (nm). Clearly, the Au(556)/TiO₂ NT, Au(556)/TiO₂ NTPC, and Au(590)/TiO₂ NTPC exhibited obvious photoactivity enhancement at the wavelength corresponding to the Au NCs SPR at 560 and 590 nm, respectively. Since the irradiation energy level within this region is much lower than the band gap of TiO₂, direct electron–hole generation from TiO₂ in this case could be ruled out, which is supported by almost zero photocurrent density on the TiO₂ NTPC under the visible light illumination. As the photoactivity enhancement peaked at the same wavelength as the characteristic plasmonic wavelength of the Au NCs, the SPR enhancement of the Au NCs under the visible light illumination was the major contributor. Furthermore, the Au(556)/TiO₂ NTPC showed much higher IPCE value than the Au(590)/TiO₂ NTPC and Au(556)/TiO₂ NT without a PC layer, confirming the role of the matching of plasmonic wavelength of Au NCs and photonic band gap of PC layer in enhancing the SPR intensity, which in turn directly improves the PEC performance.

There are four major energy-transfer mechanisms in a plasmonic–photocatalyst system:⁴² (1) hot electron transfer, (2) plasmonic heating, (3) near-field electromagnetic enhancement, and (4) resonant photon scattering. First, the effect of the plasmonic heating can be excluded since water splitting requires the energy of at least 1.23 eV, which is much higher than the thermal energy the plasmonic heating can generate.⁴³ Second, the resonant photon-scattering mechanism can also be ruled out for the Au/TiO₂ NTPC, as it normally occurs for large plasmonic nanostructures (larger than ~50 nm in diameter).^{44,45} Third, near-field electromagnetic enhancement normally is observed at wavelengths where the plasmon resonance and semiconductor absorption overlap.²⁰ In our case, we believe that the hot electron transfer mechanism is the major contributor to the enhanced PEC performance of the Au/TiO₂ NTPC under visible light illumination. As schematically presented in Figure 3c, the Au NCs essentially act as a sensitizer, absorbing resonant photons, generating the energetic hot electrons from the process of the SPR excitation, and injecting them into the conduction band of the adjacent TiO₂ NTPC.

For the purpose of further characterizing the designed photoelectrodes, the PEC performance of the Au(556)/TiO₂ NTPC was also investigated under entire solar light irradiation (AM 1.5G, intensity: 100 mW cm⁻²). Figure 4a presents linear-sweep voltammograms (LSV) under illumination of chopped light (with a frequency of 0.2 Hz) within the potential range of -0.2 to 2 V vs RHE. Clearly, both the TiO₂ NTPC and Au(556)/TiO₂ NTPC photoelectrodes exhibited fast light response, which is due to efficient charge transport through one-dimensional nanotube channels. More importantly, comparing to the photocurrent density generated on the TiO₂ NTPC (i.e., 1.22 mA cm⁻²) at 1.23 V vs RHE, the one on

the Au(556)/TiO₂ NTPC was 2.25 mA cm⁻², which is significantly higher and is comparable to the highest photocurrent density (2.5–2.6 mA cm⁻²)^{10,46} ever reported on TiO₂-based photoelectrodes under otherwise the same measurement conditions. The photocurrent density enhancement (0.15 mA cm⁻²) on the Au(556)/TiO₂ NTPC from SPR enhancement under visible light illumination alone is far short of the overall increase of the photocurrent density under illumination of the entire solar spectrum (1.03 mA cm⁻²; from 1.22 to 2.25 mA cm⁻²). The photocurrent density enhancement in the UV region was the major contributor in this case, which can be ascribed to the electronic structure modification of the TiO₂ NTPC after the Au NCs deposition (the detailed discussion on this can be found in the Supporting Information).

The photoconversion (i.e., photon-to-hydrogen) efficiencies (η) on the TiO₂ NTPC and Au(556)/TiO₂ NTPC were calculated using the following equation:

$$\eta = I(E^{\circ}_{\text{rev}} - V)/J_{\text{light}} \quad (2)$$

where I is the measured photocurrent density (mA cm^{-2}), J_{light} is the incident light irradiance (mW cm^{-2}), E°_{rev} is the standard reversible potential which is 1.23 V vs RHE, and V is the applied bias potential vs RHE (V). Figure 4b presents the plots of the photoconversion efficiencies vs applied bias potentials. The TiO₂ NTPC exhibited an optimal conversion efficiency of 0.58% while the Au(556)/TiO₂ NTPC achieved a much higher optimal conversion efficiency of 1.10% at potential of 0.5 V vs RHE. To eliminate the discrepancy between the irradiance of the light source used in lab and solar light, the corresponding IPCE spectra were measured (Figure S9) and integrated with a standard AM1.5G solar spectrum (ASTM G-173-03) using the following equation:¹⁰

$$\eta \% = \int_{300}^{700} \frac{1}{1240} \lambda (1.23 - V_{\text{bias}}) \text{IPCE}(\lambda) E(\lambda) d(\lambda) \quad (3)$$

where $E(\lambda)$ is solar irradiance at a special wavelength (λ), V_{bias} is applied bias vs RHE, and IPCE is the obtained photoresponse profiles of photoelectrodes at a specific wavelength (λ) at 0.5 V vs RHE. Figure 4c presents the photoconversion efficiencies as a function of wavelength in the range of 300–700 nm, and it can be seen that the TiO₂ NTPC and Au(556)/TiO₂ NTPC achieved photoconversion efficiency of 0.32% and 0.90%, respectively. It should be noted that the values of the photoconversion efficiencies on the Au(556)/TiO₂ NTPC estimated from two different methods, i.e., 1.1% using eq 2 and 0.90% using eq 3, are both comparable to the highest values reported on TiO₂-based photoelectrodes under otherwise the same conditions.

It is important to directly examine the evolution of H₂ and O₂ in PEC water-splitting experiment.^{47,48} For this purpose, a homemade device was fabricated, which is capable of separately collecting and measuring the volumes of the H₂ and O₂ gas generated on two electrodes (Figures S10 and S11). The results showed that under entire solar light irradiation the H₂ and O₂ were evolved at the expected stoichiometric ratio with generation rates of 27.9 μmol h⁻¹ for H₂ and 13.6 μmol h⁻¹ for O₂ within a 120 min period of testing time (Figure 4d). The photocurrent–time curve (Figure S12) was recorded during gas evolution to determine the theoretical gas production rates, and it was found that the measured rates of H₂ and O₂ evolved were slightly less than the theoretical gas production rates

presumably due to the back-reaction of dissolved oxygen reduction on Pt electrode and possible gas leakage.

In summary, plasmonic Au NCs coupled TiO₂ nanotube with top seamless photonic crystal layer showed excellent PEC water-splitting performance. The matching of the Au SPR wavelength with the PC photonic band gap significantly increased the SPR intensity and thus boosted the PEC performance. The rational design of the plasmonic–photonic crystal system paves a new avenue of preparing efficient visible light photocatalyst.

■ ASSOCIATED CONTENT

Supporting Information

Experimental section and XRD, EDS, XPS, SEM, simulation, and diffuse reflectance UV-vis spectra. This material is available free of charge via the Internet at <http://pubs.acs.org>.

■ AUTHOR INFORMATION

Corresponding Author

*E-mail peng.wang@kaust.edu.sa; Tel +966-2-8082380.

Notes

The authors declare no competing financial interest.

■ ACKNOWLEDGMENTS

The authors are grateful for KAUST for providing financial support.

■ REFERENCES

- (1) Khaselev, O.; Turner, J. A. *Science* **1998**, *280*, 425–427.
- (2) Walter, M. G.; Warren, E. L.; McKone, J. R.; Boettcher, S. W.; Mi, Q.; Santori, E. A.; Lewis, N. S. *Chem. Rev.* **2010**, *111*, 6446–6473.
- (3) Chen, X.; Shen, S.; Guo, L.; Mao, S. S. *Chem. Rev.* **2010**, *111*, 6503–6570.
- (4) Oh, I.; Kye, J.; Hwang, S. *Nano Lett.* **2012**, *12*, 298–302.
- (5) Ling, Y.; Wang, G.; Wheeler, D. A.; Zhang, J. Z.; Li, Y. *Nano Lett.* **2011**, *11*, 2119–2125.
- (6) Paracchino, A.; Laporte, V.; Sivula, K.; Gratzel, M.; Thimsen, E. *Nat. Mater.* **2011**, *10*, 456–461.
- (7) Hwang, Y. J.; Wu, C. H.; Hahn, C.; Jeong, H. E.; Yang, P. *Nano Lett.* **2012**, *12*, 1678–1682.
- (8) Zhang, Z.; Wang, P. *J. Mater. Chem.* **2012**, *22*, 2456–2464.
- (9) Wolcott, A.; Smith, W. S.; Kuykendall, T. R.; Zhao, Y.; Zhang, J. Z. *Small* **2009**, *5*, 104–111.
- (10) Wang, G.; Wang, H.; Ling, Y.; Tang, Y.; Yang, X.; Fitzmorris, R. C.; Wang, C.; Zhang, J. Z.; Li, Y. *Nano Lett.* **2011**, *11*, 3026–3033.
- (11) Zhang, Z.; Hossain, M. F.; Takahashi, T. *Int. J. Hydrogen Energy* **2010**, *35*, 8528–8535.
- (12) Cho, I. S.; Chen, Z.; Forman, A. J.; Kim, D. R.; Rao, P. M.; Jaramillo, T. F.; Zheng, X. *Nano Lett.* **2011**, *11*, 4978–4984.
- (13) Roy, P.; Berger, S.; Schmuki, P. *Angew. Chem., Int. Ed.* **2011**, *50*, 2904–2939.
- (14) Shin, Y.; Lee, S. *Nano Lett.* **2008**, *8*, 3171–3173.
- (15) Youngblood, W. J.; Lee, S. H. A.; Kobayashi, Y.; Hernandez-Pagan, E. A.; Hoerz, P. G.; Moore, T. A.; Moore, A. L.; Gust, D.; Mallouk, T. E. *J. Am. Chem. Soc.* **2009**, *131*, 926–927.
- (16) Khan, S. U. M.; Al-Shahry, M.; Ingler, W. B., Jr. *Science* **2002**, *297*, 2243–2245.
- (17) Ghicov, A.; Macak, J. M.; Tsuchiya, H.; Kunze, J.; Haeublein, V.; Frey, L.; Schmuki, P. *Nano Lett.* **2006**, *6*, 1080–1082.
- (18) Lu, N.; Quan, X.; Li, J.; Chen, S.; Yu, H.; Chen, G. *J. Phys. Chem. C* **2007**, *111*, 11836–11842.
- (19) Park, J. H.; Kim, S.; Bard, A. J. *Nano Lett.* **2006**, *6*, 24–28.
- (20) Warren, S. C.; Thimsen, E. *Energy Environ. Sci.* **2012**, *5*, 5133–5146.
- (21) She, Z. W.; Liu, S.; Low, M.; Zhang, S. Y.; Liu, Z.; Mlayah, A.; Han, M. Y. *Adv. Mater.* **2012**, *24*, 2310–2314.
- (22) Tian, Y.; Tatsuma, T. *J. Am. Chem. Soc.* **2005**, *127*, 7632–7637.
- (23) Mubeen, S.; Hernandez-Sosa, G.; Moses, D.; Lee, J.; Moskovits, M. *Nano Lett.* **2011**, *11*, 5548–5552.
- (24) Yip, C. T.; Huang, H.; Zhou, L.; Xie, K.; Wang, Y.; Feng, T.; Li, J.; Tam, W. Y. *Adv. Mater.* **2011**, *23*, 5624–5628.
- (25) Guldin, S.; Hüttner, S.; Kolle, M.; Welland, M. E.; Müller-Buschbaum, P.; Friend, R. H.; Steiner, U.; Tétreault, N. *Nano Lett.* **2010**, *10*, 2303–2309.
- (26) Colodrero, S.; Mihi, A.; Haggman, L.; Ocana, M.; Boschloo, G.; Hagfeldt, A.; Miguez, H. *Adv. Mater.* **2009**, *21*, 764–770.
- (27) Wang, X. D.; Neff, C.; Graugnard, E.; Ding, Y.; King, J. S.; Pranger, L. A.; Tannenbaum, R.; Wang, Z. L.; Summers, C. J. *Adv. Mater.* **2005**, *17*, 2103–2106.
- (28) Halaoui, L. I.; Abrams, N. M.; Mallouk, T. E. *J. Phys. Chem. B* **2005**, *109*, 6334–6342.
- (29) Nishimura, S.; Abrams, N.; Lewis, B. A.; Halaoui, L. I.; Mallouk, T. E.; Benkstein, K. D.; van de Lagemaat, J.; Frank, A. J. *J. Am. Chem. Soc.* **2003**, *125*, 6306–6310.
- (30) Zhang, Z.; Wang, P. *Energy Environ. Sci.* **2012**, *5*, 6506–6512.
- (31) Zhang, Z.; Yu, Y.; Wang, P. *ACS Appl. Mater. Interfaces* **2012**, *4*, 990–996.
- (32) Wang, F.; Liu, Y.; Dong, W.; Shen, M.; Kang, Z. *J. Phys. Chem. C* **2011**, *115*, 14635–14640.
- (33) Ye, M.; Xin, X.; Lin, C.; Lin, Z. *Nano Lett.* **2011**, *11*, 3214–3220.
- (34) Lynch, R. P.; Ghicov, A.; Schmuki, P. *J. Electrochem. Soc.* **2010**, *157*, G76–G84.
- (35) Takahashi, M.; Tsukigi, K.; Uchino, T.; Yoko, T. *Thin Solid Films* **2001**, *388*, 231–236.
- (36) Fuggle, J. C.; Martensson, N. J. *Electron Spectrosc. Relat. Phenom.* **1980**, *21*, 275–281.
- (37) Kruse, N.; Chenakin, S. *Appl. Catal. A: Gen.* **2011**, *391*, 367–376.
- (38) Tian, Y.; Tatsuma, T. *Chem. Commun.* **2004**, 1810–1811.
- (39) Yu, K.; Tian, Y.; Tatsuma, T. *Chem. Commun.* **2006**, *8*, 5417–5420.
- (40) Naseri, N.; Amiri, M.; Moshfegh, A. Z. *J. Phys. D: Appl. Phys.* **2010**, *43*, 105405–105412.
- (41) Naseri, N.; Sangpour, P.; Moshfegh, A. Z. *Electrochim. Acta* **2011**, *56*, 1150–1158.
- (42) Linic, S.; Christopher, P.; Ingram, D. B. *Nat. Mater.* **2011**, *10*, 911–921.
- (43) Liu, Z.; Hou, W.; Pavaskar, P.; Aykol, M.; Cronin, S. B. *Nano Lett.* **2011**, *11*, 1111–1116.
- (44) Burda, C.; Chen, X.; Narayanan, R.; El-Sayed, M. A. *Chem. Rev.* **2005**, *105*, 1025–1102.
- (45) Evanoff, D. D.; Chumanov, G. *ChemPhysChem* **2005**, *6*, 1221–1231.
- (46) Liu, M.; de Leon Snapp, N.; Park, H. *Chem. Sci.* **2011**, *2*, 80–87.
- (47) Maeda, K.; Higashi, M.; Siritanaratkul, B.; Abe, R.; Domen, K. *J. Am. Chem. Soc.* **2011**, *133*, 12334–12337.
- (48) Higashi, M.; Domen, K.; Abe, R. *J. Am. Chem. Soc.* **2012**, *134*, 6968–6971.